ACS Catalysis

Research Article

Cite This: ACS Catal. 2018, 8, 3825−3832

pubs.acs.org/acscatalysis

Role of Carbonaceous Aerosols in Catalyzing Sulfate Formation

Guangzhi He,[†,‡,∥] Jinzhu Ma,[†,‡,§,∥] and Hong He*[,†,‡,§]

[†]State Key Joint Laboratory of Environment Simulation and Pollution Control, Research Center for Eco-Environmental Sciences, Chinese Academy of Sciences, Beijing 100085, People's Republic of China

[‡]University of Chinese Academy of Sciences, Beijing 100049, People's Republic of China

[§]Center for Excellence in Regional Atmospheric Environment, Institute of Urban Environment, Chinese Academy of Sciences, Xiamen 361021, People's Republic of China

Supporting Information

ABSTRACT: The persistent and fast formation of sulfate is a primary factor driving the explosive growth of fine particles and exacerbating China's severe haze development. However, the underlying mechanism for the persistent production of sulfate remains highly uncertain. Here, we demonstrate that soot is not only a major component of the particulate matter but also a natural carbocatalyst to activate molecular O_2 and catalyze the oxidation of SO_2 to sulfate under ambient conditions. Moreover, high relative humidity, typically occurring in severe haze events, can greatly accelerate the catalytic cycle by reducing the reaction barriers, leading to faster sulfate production. The formation pathway of sulfate catalyzed by carbonaceous soot aerosols uses the ubiquitous O_2 as the ultimate oxidant and can proceed at night when photochemistry is reduced. The high relative humidity during haze episodes can further promote the soot-catalyzed sulfate-producing process. Therefore, this study reveals a missing and widespread source for the persistent sulfate haze formation in the open atmosphere, particularly under highly polluted conditions characterized by high concentrations of both SO_2 and particulate carbon, and is helpful to the development of more efficient policies to mitigate and control haze pollution.

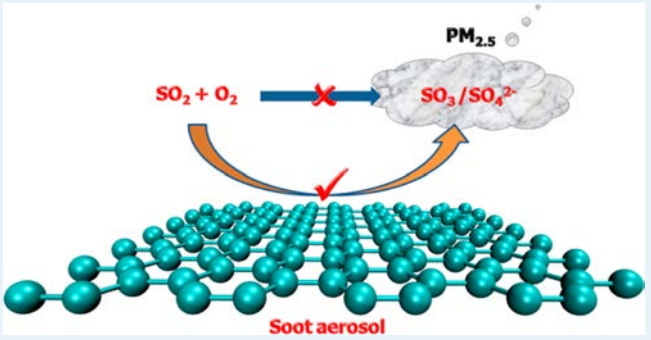

KEYWORDS: *carbocatalyst, O_2 activation, catalytic oxidation of SO_2, sources of sulfate, secondary aerosols, haze formation, first-principles calculations*

1. INTRODUCTION

In China, extremely severe and persistent haze pollution has been a serious environmental problem that causes the deterioration of air quality and regional climate change and threatens the health of hundreds of millions of people.[1,2] An outstanding feature of the fine haze particles is the high secondary aerosol contribution (up to 60−70% of $PM_{2.5}$), especially sulfate.[1,3−9] Sulfate is the fastest-forming species and rapidly becomes the main component of secondary aerosols during the evolution of haze.[6,8,10] It was observed that sulfate production rates were 6 times higher during severe haze episodes in comparison to clean episodes in the Beijing haze event of January 2013.[11] The formation of sulfate is therefore considered as a primary factor driving the explosive growth of fine particles and exacerbating severe haze development. However, current air quality models that have implemented the oxidation of SO_2 by OH radical, H_2O_2, and O_3 fail to reproduce the exceedingly high levels of sulfate under polluted conditions.[9,11,12] Moreover, photochemical oxidants, such as OH radical and O_3, are significantly reduced during haze episodes due to the aerosol dimming effect. Therefore, the remarkable and puzzling gap between modeled and observed sulfate implies the existence of large missing sources of sulfate. At present, the predominant sulfur oxidation mechanisms leading to heavy haze pollution remain uncertain, hindering the development of efficient policies to mitigate its regional and global effects.

High particulate matter levels associated with high gaseous pollutant and water vapor concentrations are typical features of atmospheric chemistry in haze pollution episodes, which provide the necessary conditions for heterogeneous reactions. Moreover, the enhanced stagnation of air under polluted conditions is conducive to trapping of pollutants and water at the surface.[11,13] Extensive studies have indicated that the heterogeneous processes on particle surfaces play an important role in the production of secondary aerosols and haze formation, such as the synergistic oxidation of SO_2 and NO_2 on the surfaces of mineral aerosols[6] and the aqueous oxidation of SO_2 by NO_2 in aerosol water under high relative humidity and neutralization conditions.[5,11] Novakov et al. first exper-

Received: December 7, 2017
Revised: March 23, 2018
Published: March 27, 2018

DOI: 10.1021/acscatal.7b04195
ACS Catal. 2018, 8, 3825−3832

imentally observed that soot particles could catalyze the oxidation of SO_2 to sulfate.[14] Our previous studies demonstrated that soot can catalyze the sunlight-irradiated photooxidation of organic carbon by O_2.[15] These experimental observations imply that soot particles may have a significant effect on the activation of molecular O_2 and the conversion of SO_2 to sulfate. Soot, produced from the incomplete combustion of fossil fuel and biomass, contributes 10−50% of the total tropospheric particulate matter.[16] Rapid economic development and accelerating industrialization has been accompanied by high emissions of soot particles in China (up to about 2.0 Tg/yr,[17] more than one-fourth of global emissions[18,19]). A soot mass concentration of up to 20 $\mu g/m^3$ was observed during the pollution events in north China.[1] However, the mechanism for the soot-catalyzed oxidation of SO_2 to sulfate is unknown.

Here, by means of first-principles calculations and IR spectra, we identify the catalytic centers for O_2 activation and SO_2 oxidation on carbonaceous soot particles and then elucidate the mechanism of SO_2 conversion to sulfate catalyzed by soot.

2. EXPERIMENTAL SECTION

2.1. Soot Production and Characterization. Soot samples were produced by burning *n*-hexane (AR, Sinopharm Chemical Reagent Co.) in a coflow homemade diffusion burner. This burner consisted of a diffusion flame that was maintained in a synthetic airflow (80% N_2 + 20% O_2), which was controlled by mass flow controllers to regulate the fuel/oxygen ratio. The fuel was fed by a cotton wick extending into the liquid fuel reservoir. The combustion conditions were expressed as the molar ratio of the consumed fuel (measured by the mass of consumed *n*-hexane) to the introduced oxygen (obtained from the entrained airflow volume) during the combustion process. The fuel/oxygen ratio was maintained at 0.16, and the obtained soot was identified as fuel-rich flame soot according to our previous studies.[15,20] The organic carbon (OC) content of soot samples was characterized using thermogravimetric analysis (TGA) with a TGA/DSC1 STAR^e system (Mettler Toledo). About 5 mg of soot was heated to 300 °C under 100 mL/min N_2 flow at a heating rate of 10 °C/min. The mass content of OC of the as-prepared soot was estimated to be 9.4 ± 0.9% (n = 4) (see Figure S1).

2.2. ATR-IR Measurements. The in situ attenuated total internal reflection infrared spectra (ATR-IR) were recorded using a NEXUS 6700 (Thermo Nicolet Instrument Corp.) Fourier transform infrared (FT-IR) spectrometer equipped with a high-sensitivity mercury−cadmium−telluride (MCT) detector cooled by liquid N_2. Soot samples from the diffusion flame were directly deposited on the ZnSe crystal of the ATR-IR cell. The spectra of soot were recorded (100 scans, 4 cm^{-1} resolution) using the blank ZnSe as reference. The ATR-IR cell was sealed with quartz glass. Soot was first purged with 100 mL min^{-1} synthetic air (80% N_2 + 20% O_2) at 298 K until the infrared spectrum was unchanged. Our previous studies have demonstrated that photochemical oxidation by O_2 under sunlight irradiation is a very important aging process for soot due to the abundance of O_2 in the troposphere and its high photoreactivity rate.[15] Therefore, the soot was exposed to a synthetic air (80% N_2 + 20% O_2) flow for 24 h under Xenon lamp (500 W) irradiation to simulate the atmospheric photochemical aging process. The xenon lamp has a continuous emission in the 350−700 nm range and a dominant wavelength at 480 nm. The light of the xenon lamp was transmitted by an optical fiber located at 10 cm over the soot samples, and the total irradiance of light was 25 mW/cm^2 at the soot surface. Then we introduced 20 ppm of SO_2 flowed over the aged soot samples in the dark under different atmospheric conditions (i.e., dry N_2, dry synthetic air, and synthetic air of 35% relative humidity). The spectra of SO_2-containing gas flowed soot were subtracted by the spectra of aged soot.

2.3. Computational Details. Geometries and energies were calculated using the Perdew−Burke−Ernzerhof (PBE) functional[21] with van der Waals correction proposed by Grimme (i.e., DFT-D2 method)[22] as implemented in the Vienna ab initio simulation package (VASP 5.4.1).[23,24] The projector augmented wave method (PAW) was used to describe the interaction between the ions and the electrons.[25,26] The energy cutoff of the plane wave was set to 400 eV. A functionalized graphene plane with a rectangular boundary (17.04 × 17.22 Å; see Figure S2) was used as the substrate. The defected basal plane has been widely used to construct the carbonyl and ether groups on the graphitic carbon sheets under periodic boundary conditions.[27,28] A vacuum region of 20 Å was used to avoid the periodic image interaction normal to the surface. The Brillouin zone was sampled using a Monkhorst−Pack 2 × 2 × 1 mesh. The Gaussian smearing method with a smearing width of 0.2 eV was employed to accelerate the convergence of integration at the Brillouin zone. The reaction pathways and transition states were traced by the climbing image nudged elastic band (CI-NEB) method with a spring constant of 5.0 eV/Å^2 to restrain the images on the elastic band.[29,30] All atoms were relaxed until the forces on each atom were less than 0.02 eV/Å. No obvious differences in the structural properties (<0.01 Å) and energy barriers (<0.01 eV) were observed when k points were increased from 2 × 2 × 1 to 3 × 3 × 2 and the energy cutoff from 400 to 600 eV (see Table S1), indicating that the calculations have converged, and the computational settings used here are reliable for describing current issues. The VASPsol implicit solvation model was used to simulate the average effect of water solvent on the solute and to compute the reaction barriers under aqueous conditions. The solvation model treats the solute quantum mechanically and treats the solvent as a continuum, which is generally applicable to various molecular and extended systems.[31] A single-point calculation at the VASP-optimized geometry was performed at the M062X/6-311G(d,p) level[32,33] with the Gaussian 09 package[34] to produce a standard wave function (WFN) file. The electron localization function (ELF),[35] Mayer bond order (MBO),[36,37] and reduced density gradient (RDG)[38] were analyzed using the WFN file with the Multiwfn package.[39,40] The reaction rate constants (k) were calculated on the basis of the transition state theory formula including the Wigner tunneling correction (eq 1) using the KiSThelP code,[41] where χ is the Wigner transmission coefficient (eq 2), k_b is the Boltzmann constant, h is Planck's constant, T is the temperature, Im($\nu^{\ddagger}$) is the imaginary frequency, and ΔE is the difference in energies between the transition state and the reactant complex. The reaction rate was further estimated by the half-life ($t_{1/2}$, eq 3).

$$k = \chi \frac{k_b T}{h} \exp\left(-\frac{\Delta E}{k_b T}\right) \quad (1)$$

$$\chi = 1 + \frac{1}{24}\left(\frac{h\ \mathrm{Im}(\nu^{\ddagger})}{k_b T}\right)^2 \quad (2)$$

DOI: 10.1021/acscatal.7b04195
ACS Catal. 2018, 8, 3825−3832

$$t_{1/2} = \ln 2/k \quad (3)$$

3. RESULTS AND DISCUSSION

3.1. O_2 Activation on Soot Surfaces. Soot mainly consists of graphitic carbon, with a number of C═O and C−O oxygen-containing functional groups within the graphene sheets.[15,42−45] Once emitted into the atmosphere, soot particles undergo aging processes,[16] and the carbonyl C═O and ether C−O groups on soot surfaces increase significantly during the atmospheric photochemical aging process[15] (see Figure S3). When SO_2-containing dry air (80% N_2 + 20% O_2) was flowed over an aged soot sample in the dark, the SO_2 was oxidized to sulfate species, denoted by a rapid increase of the IR spectral intensity in the region of 990−1325 cm^{-1} (Figure 1a).

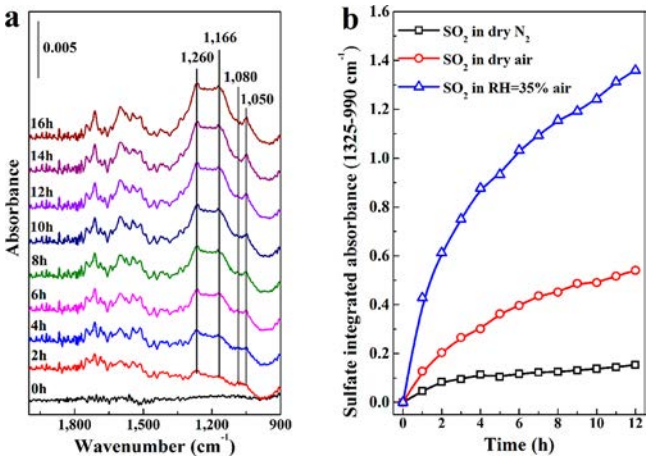

Figure 1. (a) ATR-IR spectra of soot exposed to SO_2-containing dry synthetic air (80% N_2 + 20% O_2). The absorption band in the region of 990−1325 cm^{-1} originated from the vibrations of sulfate species (see Table S2). (b) Integrated absorbance between 990 and 1325 cm^{-1} for the samples under different atmospheric conditions.

Moreover, the production of sulfate over the soot particles in the absence of O_2 was significantly lower than that under O_2 conditions (Figure 1b). The result shows an obvious catalytic effect of soot on the oxidation of SO_2 by O_2 to form sulfate. The production of sulfate was further enhanced under elevated relative humidity (RH) conditions, indicating that increasing humidity promoted the catalytic process (Figure 1b).

Determination of the active sites that enable the dissociation of unreactive O_2 to reactive atomic oxygen species under ambient conditions is the key to unraveling the mechanism of the oxidation of SO_2 catalyzed by carbonaceous soot particles. Reaction pathways of O_2 dissociation at carbonyl, ether, and pristine graphitic C sites were identified using first-principles calculations (Figure 2). At the carbonyl and pristine C sites, the O_2 molecule is dissociated and converted to two epoxide groups endothermically with rather high barriers (2.31 and 1.87 eV, respectively), implying that the reactions are prohibited under normal conditions. In contrast, the overall energy barrier for O_2 dissociation into two epoxide groups at the ether site is 0.75 eV, much lower than that at the carbonyl and pristine graphitic C sites, and is surmountable at room temperature.[46] Moreover, this process is exothermic by 0.29 eV. Therefore, the dissociation of O_2 at the ether C−O site is both thermodynamically and kinetically favorable, indicating that the ether groups are the active sites on soot for O_2 dissociation.

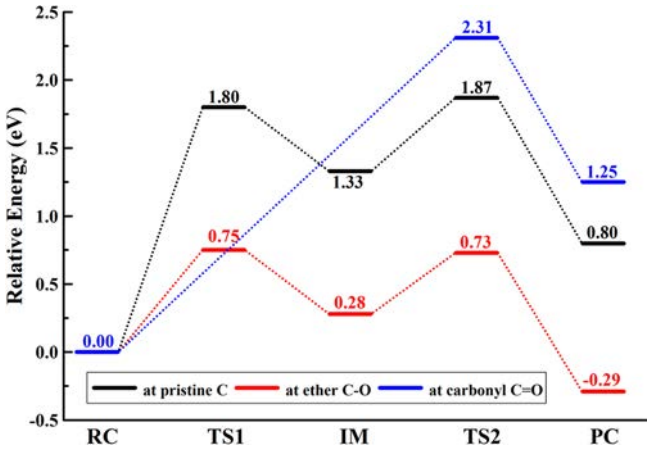

Figure 2. Energy profile of the reaction pathways of O_2 dissociation at carbonyl C═O, ether C−O, and pristine graphitic C sites. The energies are given in eV relative to the reactant complex. Abbreviations: RC, reactant complex; TS1, the first transition state; IM, intermediate species; TS2, the second transition state; PC, product complex.

The dissociation of O_2 proceeds via two steps (Figure 3). When the O_2 molecule approaches the surface ether group, it is

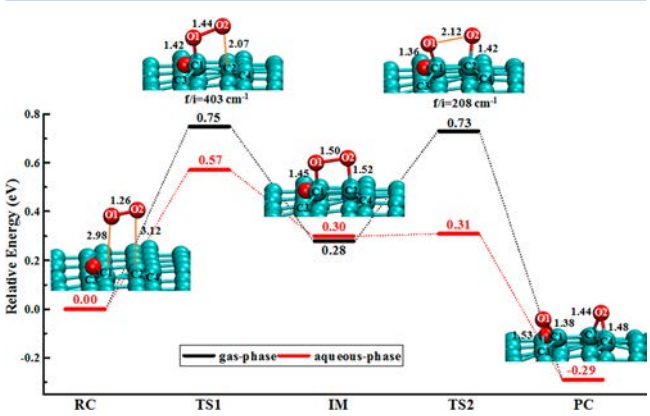

Figure 3. Gas-phase and aqueous-phase energy profiles of the reaction pathway of O_2 dissociation at the ether C−O site as well as the optimized geometries of the reactant, transition states, intermediate, and product. Red, cyan, and white circles denote O, C, and H atoms, respectively. The two C atoms bonded to the O1 atom are denoted C1 and C3, while C2 and C4 are the two C atoms bonded to the O2 atom. The imaginary frequencies of the transition states are presented. All lengths are given in Å. The optimized geometries of the reactants, transition states, intermediate, and products of O_2 dissociation at carbonyl and pristine graphitic C sites are shown in Figures S4 and S5.

first chemisorbed on the C site (named C1) of the ether group by the O1 atom, with the O1−O2 bond being elongated from 1.26 to 1.44 Å. Then, the O2 atom gets closer to the surface and forms an intermediate with a square geometry. Subsequently, the O1−O2 bond is completely broken, synchronized with the formation of C3−O1 and C4−O2 bonds. The O_2 molecule is finally converted into two epoxide groups.

Fresh soot is hydrophobic, while the aged soot particles become significantly hydrophilic and can be incorporated into existing liquid droplets or activated as cloud condensation nuclei (CCNs) in the atmosphere.[16,47] Typically, severe haze pollution episodes occur with concurrent high relative

DOI: 10.1021/acscatal.7b04195
ACS Catal. 2018, 8, 3825−3832

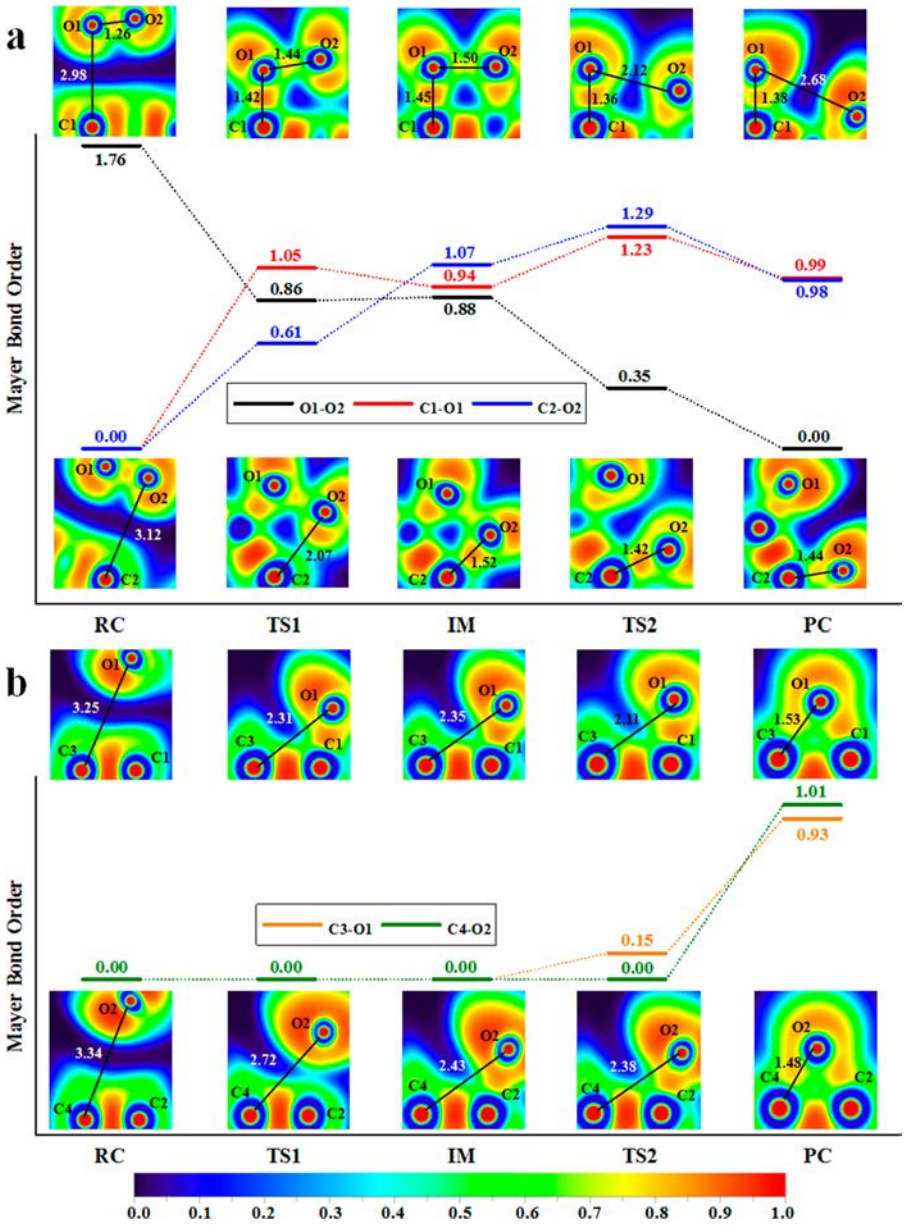

Figure 4. Mayer bond order (MBO) and two-dimensional electron localization function (ELF) color-filled maps for the minima and transition states along the pathway of O_2 dissociation at the ether C−O site. An MBO value lower than the default threshold of 0.05 is regarded as 0. The atoms used to define the plane of ELF maps are labeled. Areas beyond the interaction are omitted for clarity. All lengths are given in Å.

humidity.[5,11] Abundant aerosol water is conducive to forming aqueous solution environments at the surface of aged soot and enables reactions to take place in aqueous medium. It is notable that the overall energy barrier of O_2 dissociation at the ether site is significantly decreased to 0.57 eV in aqueous media (Figure 3), indicating that the reaction is faster under high relative humidity and aqueous conditions, which is qualitatively consistent with our experimental results (Figure 1b). According to transition state theory,[41] at 278 K (a typical temperature during the winter in north China), the half-lives ($t_{1/2}$, the time required for the reactant concentration to fall to half of its initial value) are predicted to be 4.6 s in the gas phase and 2.5×10^{-3} s in aqueous solution, showing that the O_2 dissociation at the ether C−O site is fairly easy and the reaction rate under aqueous conditions can be up to 3 orders of magnitude greater than that under gas-phase conditions. The energy barriers of O_2 dissociation are 2.09 eV at the carbonyl site and 1.68 eV at the pristine C sites in the aqueous phase (see Figures S4 and S5), both of which are significantly higher than that at the ether site and are not surmountable at room temperature. Therefore, the dissociation of O_2 at the carbonyl and pristine C sites is still unlikely to proceed in the aqueous phase.

In order to clearly characterize the bond breaking and bond formation during the reaction process, the electronic localization function (ELF) and Mayer bond order (MBO) were analyzed for the minima and transition states along the reaction pathway (Figure 4). The ELF value is in the range of 0 to 1. A high value of ELF at a given region denotes high electron localization therein and vice versa.[35] Regions of the greatest and smallest localization electron density are represented by red and blue colors, respectively.

In the first reaction step, from reactant complex to intermediate, the C1−O1 and C2−O2 MBO values increase from 0 to about 1.0, as the ELF values in their intermediate

DOI: 10.1021/acscatal.7b04195
ACS Catal. 2018, 8, 3825−3832

location increase from 0 to about 0.85, indicating that the electrons locally concentrate and form C1−O1 and C2−O2 covalent bonds (see Figure 4a). Meanwhile, the MBO value of the O1−O2 bond decreases from 1.76 to 0.88, and the corresponding ELF value in their intermediate location decreases from about 0.80 to 0.70, which suggests that the O1−O2 bond is being weakened.

As the electron density between the O1 atom and the O2 atom is further decreased as the reaction proceeds (ELF value decreased from 0.70 to 0), the O1−O2 bond is finally broken (MBO value decreased from 0.88 to 0) during the second reaction step. After the O1−O2 bond breaks, the electron localization in C3−O1 and C4−O2 intermediate locations is greatly enhanced (ELF values increased from 0 to about 0.80), showing a strong covalent interaction, which increases the C3−O1 and O4−O2 MBO values to 0.93 and 1.01, respectively, when the reaction ends at the product complex (see Figure 4b). The ELF and MBO give a good description of the O−O bond breaking and the C−O bond formation during the activation process of O_2.

3.2. Catalytic Oxidation of SO_2. The reaction pathways for the oxidation of SO_2 by the two epoxide groups generated from O_2 dissociation are presented in Figure 5, and a detailed description of the breaking of C−O bonds and the formation of S−O bonds during the reaction processes is shown in Figure S6. When the SO_2 molecule reacts with the epoxide group away from the ether site (see Figure 5a), the C2−O2 bond breaks first. Then, the SO_2 molecule continues to attack the O2 atom, synchronized with the breaking of the C4−O2 bond, leading to the formation of a SO_3 molecule. The energy barrier of this process is 0.73 eV in the gas phase, suggesting that this oxidation reaction can occur under ambient conditions. Moreover, the energy barrier is decreased to 0.47 eV in aqueous solution. At 278 K, we obtain the half-life of 2.0 s under gas-phase conditions, whereas the half-life is decreased to 3.9×10^{-5} s under aqueous conditions, showing that the oxidation of SO_2 is more rapid than the activation of O_2 in both the gas phase and solution. As shown in Figure 5b, the oxidation of SO_2 by the epoxide group connected to the ether site takes place without any energy barrier, indicating that this epoxide group is more active. When the two oxidation reactions of SO_2 to SO_3 end, a catalytic cycle is completed.

These results demonstrate that the epoxide groups are the reactive oxygen species for SO_2 oxidation, while the carbonyl groups have low reactivity for SO_2 oxidation due to the high barrier of 2.26 eV (see Figure S7). The ether sites on soot surfaces that enable the dissociation of molecular O_2 to epoxide groups under ambient conditions constitute the catalytic centers for SO_2 oxidation. According to the energy barriers and half-lives, both the activation of molecular O_2 and the oxidation of SO_2 catalyzed by soot are easy and rapid. The rate-determining step in the catalytic cycle is the dissociation of O_2 in both the gas phase and solution, and the whole catalytic cycle can be greatly promoted in solution environments. This promotion mechanism is consistent with the experimental observations of the heterogeneous oxidation of SO_2.[5,11,48] The higher the polarity of the solute, the more negative the solvation energy in polar aqueous solvents. Therefore, the promotion results from the higher polarity of the transition states relative to the reactants in the reactions above.

It is well-known that the SO_3 can be facilely converted into H_2SO_4 by reaction with a water molecule, especially under high relative humidity conditions.[10,49−51] The reduced density

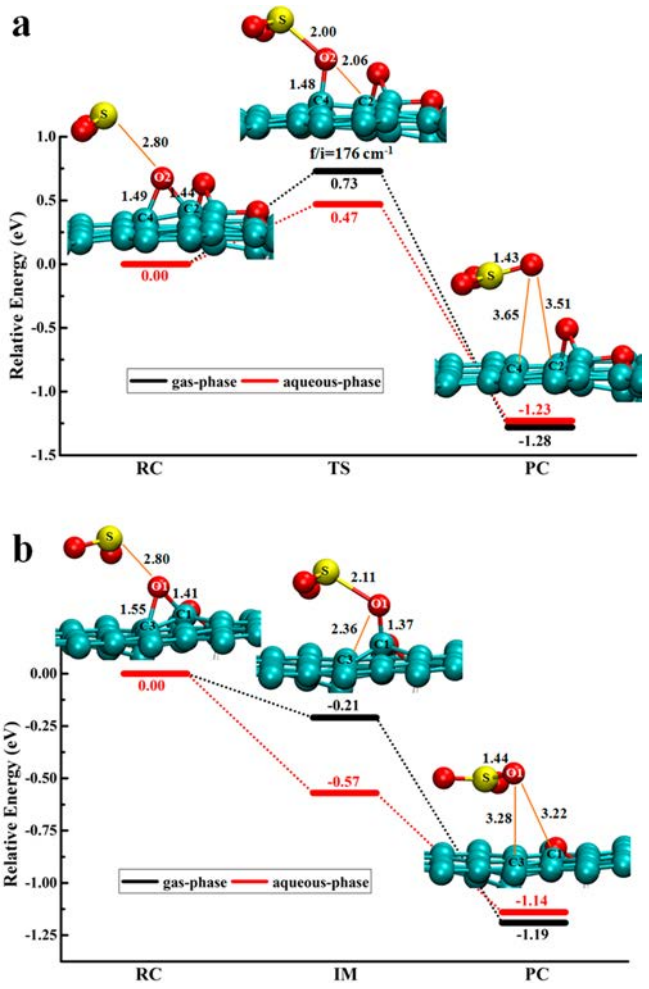

Figure 5. Gas-phase and aqueous-phase energy profiles of the reaction pathways of SO_2 oxidation by the epoxide group away from the ether C−O site (a) and by the epoxide group connected to the ether C−O site (b) as well as the optimized geometries of the reactant, transition state, and product. Yellow circles denote S atoms, and other legends are the same as those in Figure 3.

gradient of the electron density (RDG(r)), defined as $|\nabla\rho(r)/\rho^{4/3}(r)|$,[38] was analyzed to identify the nature of the interaction of formed SO_3 and H_2SO_4 species with the carbonaceous surfaces (Figure 6). The shortest interatomic distances from SO_3 and H_2SO_4 to the substrates are greater than 2.2 Å, and there is a significant green region between the SO_3/H_2SO_4 molecule and the surfaces, clearly indicating that the formed SO_3 and H_2SO_4 interact with the surfaces mainly through weak van der Waals forces. The calculated interaction energies of SO_3 and H_2SO_4 with the substrate are 0.38 and 0.34 eV, respectively, typically 1 order of magnitude smaller than that of the chemical interaction. The low affinity for the formed SO_3 and sulfate species allows the soot to maintain a long catalyst lifetime.

4. CONCLUSION

Our study reveals the mechanism of carbonaceous soot aerosol-catalyzed persistent sulfate formation, where soot is not only a major component of the particulate matter in the atmosphere but also an important catalyst to activate molecular O_2 and catalyze the conversion of SO_2 to sulfate under ambient conditions. The catalytic oxidation of SO_2 by soot aerosols uses

DOI: 10.1021/acscatal.7b04195
ACS Catal. 2018, 8, 3825−3832

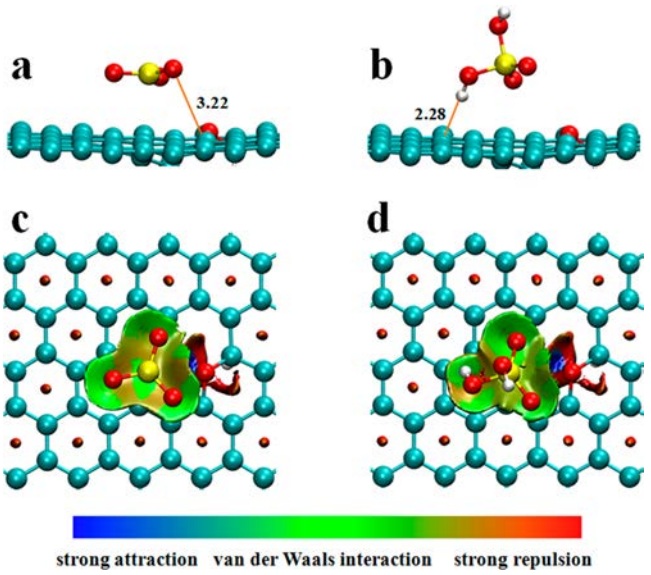

Figure 6. Optimized geometries (side view) and RDG isosurfaces colored by the values of sign[$\lambda_2(r)$]$\rho(r)$ (top view). (a) and (c) show SO_3 interacting with the substrate. (b) and (d) show H_2SO_4 interacting with the substrate. λ_2 is the second largest eigenvalue of a Hessian matrix of the electron density. The color bar shows the blue−green−red scale ranging from −0.04 to 0.02 au. Blue, green, and red represent the strong attraction (e.g., hydrogen bonding), van der Waals interaction, and strong repulsion (e.g., steric repulsion), respectively. Areas beyond the interaction are omitted for clarity. All other legends are the same as those in Figure 5.

the ubiquitous O_2 as the ultimate oxidant, and could proceed at night when photochemistry is reduced. Moreover, the reaction can be further accelerated by the high relative humidity under haze pollution conditions, leading to faster sulfate production and hence more severe haze. Thus, we believe that the principle of soot-catalyzed sulfate formation and its acceleration driven by humidity described here may play an important role in the open atmosphere and especially under polluted conditions, where both SO_2 and soot concentrations and relative humidity are high. This study will help us to develop more efficient policies to mitigate and control the severe haze pollution occurring in China and much of the developing world, because reductions of soot emissions from industry and traffic are expected to reduce haze more efficiently than previously anticipated.

Soot particles would be coated with organic and inorganic species and undergo morphology variations during the atmospheric aging processes,[52−55] which may enhance or reduce their catalytic reactivity for SO_2 oxidation. The thermogravimetric analysis (9.4 ± 0.9 wt %, Figure S1) and ATR-FTIR data (vibrations of C−H species in the range of 750−900 cm^{-1}, Figure S3) show the existence of organics in the as-prepared soot samples. However, we did not observe obvious adverse effects of the organics on the catalytic reactivity of soot for SO_2 oxidation (Figure 1). Moreover, the photooxidation of organics has been demonstrated as a source of the ether groups on soot surfaces.[15] Soot can also engage in reactions with other inorganic species, such as NO_2, under atmospheric conditions.[56] Whether there is a competition for the active sites or a synergistic effect between SO_2 and NO_2 on the surfaces of soot aerosols needs to be carefully investigated in future studies.

■ ASSOCIATED CONTENT

Supporting Information

The Supporting Information is available free of charge on the ACS Publications website at DOI: 10.1021/acscatal.7b04195.

Thermogravimetric (TG) curves of our soot samples, entire structures of the model substrates, ATR-IR spectra of fresh and photochemically aged soot, reaction pathway of O_2 dissociation at the carbonyl C═O site, reaction pathway of O_2 dissociation at the pristine graphitic C site, MBO and two-dimensional ELF color-filled maps for the minima and transition states along the pathways of SO_2 oxidation by the epoxide groups, reaction pathway of SO_2 oxidation by the carbonyl C═O group, calculated structural parameters and energy barriers (ΔE) of O_2 dissociation at the ether C−O site with different computational settings, and calculated and experimentally measured vibrational frequencies of various functional groups and sulfate species (PDF)

■ AUTHOR INFORMATION

Corresponding Author

*E-mail for H.H.: honghe@rcees.ac.cn.

ORCID

Guangzhi He: 0000-0003-1770-3522

Author Contributions

‖G.H. and J.M. contributed equally to this work.

Notes

The authors declare no competing financial interest.

■ ACKNOWLEDGMENTS

This work was supported by the National Key R&D Program of China (2016YFC0202701), the National Natural Science Foundation of China (21777171), the Major Program of National Natural Science Foundation (91543109), and the Youth Innovation Promotion Association, CAS (2017064).

■ REFERENCES

(1) Huang, R.-J.; Zhang, Y.; Bozzetti, C.; Ho, K.-F.; Cao, J.-J.; Han, Y.; Daellenbach, K. R.; Slowik, J. G.; Platt, S. M.; Canonaco, F.; Zotter, P.; Wolf, R.; Pieber, S. M.; Bruns, E. A.; Crippa, M.; Ciarelli, G.; Piazzalunga, A.; Schwikowski, M.; Abbaszade, G.; Schnelle-Kreis, J.; Zimmermann, R.; An, Z.; Szidat, S.; Baltensperger, U.; El Haddad, I.; Prevot, A. S. H. High secondary aerosol contribution to particulate pollution during haze events in China. *Nature* **2014**, *514*, 218−222.

(2) Cao, C.; Lee, X.; Liu, S.; Schultz, N.; Xiao, W.; Zhang, M.; Zhao, L. Urban heat islands in China enhanced by haze pollution. *Nat. Commun.* **2016**, *7*, 12509.

(3) Guo, S.; Hu, M.; Zamora, M. L.; Peng, J.; Shang, D.; Zheng, J.; Du, Z.; Wu, Z.; Shao, M.; Zeng, L.; Molina, M. J.; Zhang, R. Elucidating severe urban haze formation in China. *Proc. Natl. Acad. Sci. U. S. A.* **2014**, *111*, 17373−17378.

(4) Hua, W.; Verreault, D.; Allen, H. C. Relative order of sulfuric acid, bisulfate, hydronium, and cations at the air−water Interface. *J. Am. Chem. Soc.* **2015**, *137*, 13920−13926.

(5) Wang, G.; Zhang, R.; Gomez, M. E.; Yang, L.; Zamora, M. L.; Hu, M.; Lin, Y.; Peng, J.; Guo, S.; Meng, J.; Li, J.; Cheng, C.; Hu, T.; Ren, Y.; Wang, Y.; Gao, J.; Cao, J.; An, Z.; Zhou, W.; Li, G.; Wang, J.; Tian, P.; Marrero-Ortiz, W.; Secrest, J.; Du, Z.; Zheng, J.; Shang, D.; Zeng, L.; Shao, M.; Wang, W.; Huang, Y.; Wang, Y.; Zhu, Y.; Li, Y.; Hu, J.; Pan, B.; Cai, L.; Cheng, Y.; Ji, Y.; Zhang, F.; Rosenfeld, D.; Liss, P. S.; Duce, R. A.; Kolb, C. E.; Molina, M. J. Persistent sulfate formation from London Fog to Chinese haze. *Proc. Natl. Acad. Sci. U. S. A.* **2016**, *113*, 13630−13635.

DOI: 10.1021/acscatal.7b04195
ACS Catal. 2018, 8, 3825−3832

(6) He, H.; Wang, Y.; Ma, Q.; Ma, J.; Chu, B.; Ji, D.; Tang, G.; Liu, C.; Zhang, H.; Hao, J. Mineral dust and NO_x promote the conversion of SO_2 to sulfate in heavy pollution days. *Sci. Rep.* **2014**, *4*, 4172.
(7) Zheng, G.; Duan, F.; Su, H.; Ma, Y.; Cheng, Y.; Zheng, B.; Zhang, Q.; Huang, T.; Kimoto, T.; Chang, D.; Poeschl, U.; Cheng, Y.; He, K. Exploring the severe winter haze in Beijing: the impact of synoptic weather, regional transport and heterogeneous reactions. *Atmos. Chem. Phys.* **2015**, *15*, 2969−2983.
(8) Sun, Y.; Chen, C.; Zhang, Y.; Xu, W.; Zhou, L.; Cheng, X.; Zheng, H.; Ji, D.; Li, J.; Tang, X.; Fu, P.; Wang, Z. Rapid formation and evolution of an extreme haze episode in Northern China during winter 2015. *Sci. Rep.* **2016**, *6*, 27151.
(9) Wang, Y.; Zhang, Q.; Jiang, J.; Zhou, W.; Wang, B.; He, K.; Duan, F.; Zhang, Q.; Philip, S.; Xie, Y. Enhanced sulfate formation during China's severe winter haze episode in January 2013 missing from current models. *J. Geophys. Res. Atmos.* **2014**, *119*, 10,425.
(10) Li, L.; Kumar, M.; Zhu, C.; Zhong, J.; Francisco, J. S.; Zeng, X. C. Near-barrierless ammonium bisulfate formation via a loop-structure promoted proton-transfer mechanism on the surface of water. *J. Am. Chem. Soc.* **2016**, *138*, 1816−1819.
(11) Cheng, Y.; Zheng, G.; Wei, C.; Mu, Q.; Zheng, B.; Wang, Z.; Gao, M.; Zhang, Q.; He, K.; Carmichael, G.; Poschl, U.; Su, H. Reactive nitrogen chemistry in aerosol water as a source of sulfate during haze events in China. *Sci. Adv.* **2016**, *2*, e1601530.
(12) Zheng, B.; Zhang, Q.; Zhang, Y.; He, K. B.; Wang, K.; Zheng, G. J.; Duan, F. K.; Ma, Y. L.; Kimoto, T. Heterogeneous chemistry: a mechanism missing in current models to explain secondary inorganic aerosol formation during the January 2013 haze episode in North China. *Atmos. Chem. Phys.* **2015**, *15*, 2031−2049.
(13) Yang, Y.; Russell, L. M.; Lou, S.; Liao, H.; Guo, J.; Liu, Y.; Singh, B.; Ghan, S. J. Dust-wind interactions can intensify aerosol pollution over eastern China. *Nat. Commun.* **2017**, *8*, 15333.
(14) Novakov, T.; Chang, S. G.; Harker, A. B. Sulfates as pollution particulates: Catalytic formation on carbon (soot) particles. *Science* **1974**, *186*, 259−261.
(15) Han, C.; Liu, Y.; Ma, J.; He, H. Key role of organic carbon in the sunlight-enhanced atmospheric aging of soot by O_2. *Proc. Natl. Acad. Sci. U. S. A.* **2012**, *109*, 21250−21255.
(16) Zhang, R.; Khalizov, A. F.; Pagels, J.; Zhang, D.; Xue, H.; McMurry, P. H. Variability in morphology, hygroscopicity, and optical properties of soot aerosols during atmospheric processing. *Proc. Natl. Acad. Sci. U. S. A.* **2008**, *105*, 10291−10296.
(17) Wang, R.; Tao, S.; Wang, W.; Liu, J.; Shen, H.; Shen, G.; Wang, B.; Liu, X.; Li, W.; Huang, Y.; Zhang, Y.; Lu, Y.; Chen, H.; Chen, Y.; Wang, C.; Zhu, D.; Wang, X.; Li, B.; Liu, W.; Ma, J. Black carbon emissions in China from 1949 to 2050. *Environ. Sci. Technol.* **2012**, *46*, 7595−7603.
(18) Monge, M. E.; D'Anna, B.; Mazri, L.; Giroir-Fendler, A.; Ammann, M.; Donaldson, D. J.; George, C. Light changes the atmospheric reactivity of soot. *Proc. Natl. Acad. Sci. U. S. A.* **2010**, *107*, 6605−6609.
(19) Bond, T. C.; Streets, D. G.; Yarber, K. F.; Nelson, S. M.; Woo, J. H.; Klimont, Z. A technology-based global inventory of black and organic carbon emissions from combustion. *J. Geophys. Res.* **2004**, *109*, D14203.
(20) Han, C.; Liu, Y.; Liu, C.; Ma, J.; He, H. Influence of combustion conditions on hydrophilic properties and microstructure of flame soot. *J. Phys. Chem. A* **2012**, *116*, 4129−4136.
(21) Perdew, J. P.; Burke, K.; Ernzerhof, M. Generalized gradient approximation made simple. *Phys. Rev. Lett.* **1996**, *77*, 3865−3868.
(22) Grimme, S. Semiempirical GGA-type density functional constructed with a long-range dispersion correction. *J. Comput. Chem.* **2006**, *27*, 1787−1799.
(23) Kresse, G.; Furthmuller, J. Efficient iterative schemes for ab initio total-energy calculations using a plane-wave basis set. *Phys. Rev. B: Condens. Matter Mater. Phys.* **1996**, *54*, 11169−11186.
(24) Kresse, G.; Furthmuller, J. Efficiency of ab-initio total energy calculations for metals and semiconductors using a plane-wave basis set. *Comput. Mater. Sci.* **1996**, *6*, 15−50.
(25) Kresse, G.; Joubert, D. From ultrasoft pseudopotentials to the projector augmented-wave method. *Phys. Rev. B: Condens. Matter Mater. Phys.* **1999**, *59*, 1758−1775.
(26) Blochl, P. E. Projector augmented-wave method. *Phys. Rev. B: Condens. Matter Mater. Phys.* **1994**, *50*, 17953−17979.
(27) Bagri, A.; Mattevi, C.; Acik, M.; Chabal, Y. J.; Chhowalla, M.; Shenoy, V. B. Structural evolution during the reduction of chemically derived graphene oxide. *Nat. Chem.* **2010**, *2*, 581−587.
(28) Acik, M.; Mattevi, C.; Gong, C.; Lee, G.; Cho, K.; Chhowalla, M.; Chabal, Y. J. The Role of Intercalated Water in Multilayered Graphene Oxide. *ACS Nano* **2010**, *4*, 5861−5868.
(29) Henkelman, G.; Uberuaga, B. P.; Jonsson, H. A climbing image nudged elastic band method for finding saddle points and minimum energy paths. *J. Chem. Phys.* **2000**, *113*, 9901−9904.
(30) Henkelman, G.; Jonsson, H. Improved tangent estimate in the nudged elastic band method for finding minimum energy paths and saddle points. *J. Chem. Phys.* **2000**, *113*, 9978−9985.
(31) Mathew, K.; Sundararaman, R.; Letchworth-Weaver, K.; Arias, T. A.; Hennig, R. G. Implicit solvation model for density-functional study of nanocrystal surfaces and reaction pathways. *J. Chem. Phys.* **2014**, *140*, 084106.
(32) Zhao, Y.; Truhlar, D. G. The M06 suite of density functionals for main group thermochemistry, thermochemical kinetics, noncovalent interactions, excited states, and transition elements: two new functionals and systematic testing of four M06-class functionals and 12 other functionals. *Theor. Chem. Acc.* **2008**, *120*, 215−241.
(33) Krishnan, R.; Binkley, J. S.; Seeger, R.; Pople, J. A. Self-consistent molecular orbital methods. XX. A basis set for correlated wave functions. *J. Chem. Phys.* **1980**, *72*, 650−654.
(34) Frisch, M. J.; Trucks, G. W.; Schlegel, H. B.; Scuseria, G. E.; Robb, M. A.; Cheeseman, J. R.; Scalmani, G.; Barone, V.; Mennucci, B.; Petersson, G. A.; Nakatsuji, H.; Caricato, M.; Li, X.; Hratchian, H. P.; Izmaylov, A. F.; Bloino, J.; Zheng, G.; Sonnenberg, J. L.; Hada, M.; Ehara, M.; Toyota, K.; Fukuda, R.; Hasegawa, J.; Ishida, M.; Nakajima, T.; Honda, Y.; Kitao, O.; Nakai, H.; Vreven, T.; Montgomery, J. A., Jr.; Peralta, J. E.; Ogliaro, F.; Bearpark, M.; Heyd, J. J.; Brothers, E.; Kudin, K. N.; Staroverov, V. N.; Kobayashi, R.; Normand, J.; Raghavachari, K.; Rendell, A.; Burant, J. C.; Iyengar, S. S.; Tomasi, J.; Cossi, M.; Rega, N.; Millam, N. J.; Klene, M.; Knox, J. E.; Cross, J. B.; Bakken, V.; Adamo, C.; Jaramillo, J.; Gomperts, R.; Stratmann, R. E.; Yazyev, O.; Austin, A. J.; Cammi, R.; Pomelli, C.; Ochterski, J. W.; Martin, R. L.; Morokuma, K.; Zakrzewski, V. G.; Voth, G. A.; Salvador, P.; Dannenberg, J. J.; Dapprich, S.; Daniels, A. D.; Farkas, O.; Foresman, J. B.; Ortiz, J. V.; Cioslowski, J.; Fox, D. J. *Gaussian 09, Revision D.01*; Gaussian, Inc., Wallingford, CT, 2013.
(35) Becke, A. D.; Edgecombe, K. E. A simple measure of electron localization in atomic and molecular-systems. *J. Chem. Phys.* **1990**, *92*, 5397−5403.
(36) Bridgeman, A. J.; Cavigliasso, G.; Ireland, L. R.; Rothery, J. The Mayer bond order as a tool in inorganic chemistry. *J. Chem. Soc., Dalton Trans.* **2001**, 2095−2108.
(37) Mayer, I. Charge, bond order and valence in the ab initio SCF theory. *Chem. Phys. Lett.* **1983**, *97*, 270−274.
(38) Johnson, E. R.; Keinan, S.; Mori-Sanchez, P.; Contreras-Garcia, J.; Cohen, A. J.; Yang, W. Revealing noncovalent interactions. *J. Am. Chem. Soc.* **2010**, *132*, 6498−6506.
(39) Lu, T.; Chen, F. Multiwfn: a multifunctional wavefunction analyzer. *J. Comput. Chem.* **2012**, *33*, 580−592.
(40) He, G.; He, H. DFT studies on the heterogeneous oxidation of SO_2 by oxygen functional groups on graphene. *Phys. Chem. Chem. Phys.* **2016**, *18*, 31691−31697.
(41) Canneaux, S.; Bohr, F.; Henon, E. KiSThelP: a program to predict thermodynamic properties and rate constants from quantum chemistry results. *J. Comput. Chem.* **2014**, *35*, 82−93.
(42) Cain, J. P.; Gassman, P. L.; Wang, H.; Laskin, A. Micro-FTIR study of soot chemical composition-evidence of aliphatic hydrocarbons on nascent soot surfaces. *Phys. Chem. Chem. Phys.* **2010**, *12*, 5206−5218.

DOI: 10.1021/acscatal.7b04195
ACS Catal. 2018, 8, 3825−3832

(43) Daly, H. M.; Horn, A. B. Heterogeneous chemistry of toluene, kerosene and diesel soots. *Phys. Chem. Chem. Phys.* **2009**, *11*, 1069−1076.
(44) Williams, S. Surface intermediates, mechanism, and reactivity of soot oxidation. Ph.D. Thesis, University of Toronto, Toronto, Ontario, Canada, 2008.
(45) Adler, G.; Riziq, A. A.; Erlick, C.; Rudich, Y. Effect of intrinsic organic carbon on the optical properties of fresh diesel soot. *Proc. Natl. Acad. Sci. U. S. A.* **2010**, *107*, 6699−6704.
(46) Young, D. C. In *Computational chemistry: a practical guide for applying techniques to real-world problems*; Wiley: Hoboken, NJ, 2002; pp 145−158.
(47) Zuberi, B.; Johnson, K. S.; Aleks, G. K.; Molina, L. T.; Laskin, A. Hydrophilic properties of aged soot. *Geophys. Res. Lett.* **2005**, *32*, L01807.
(48) Long, Y.; Zhang, C.; Wang, X.; Gao, J.; Wang, W.; Liu, Y. Oxidation of SO_2 to SO_3 catalyzed by graphene oxide foams. *J. Mater. Chem.* **2011**, *21*, 13934−13941.
(49) Loerting, T.; Liedl, K. R. Toward elimination of discrepancies between theory and experiment: The rate constant of the atmospheric conversion of SO_3 to H_2SO_4. *Proc. Natl. Acad. Sci. U. S. A.* **2000**, *97*, 8874−8878.
(50) Jayne, J. T.; Poschl, U.; Chen, Y. M.; Dai, D.; Molina, L. T.; Worsnop, D. R.; Kolb, C. E.; Molina, M. J. Pressure and temperature dependence of the gas-phase reaction of SO_3 with H_2O and the heterogeneous reaction of SO_3 with H_2O/H_2SO_4 surfaces. *J. Phys. Chem. A* **1997**, *101*, 10000−10011.
(51) Hazra, M. K.; Sinha, A. Formic acid catalyzed hydrolysis of SO_3 in the gas phase: a barrierless mechanism for sulfuric acid production of potential atmospheric importance. *J. Am. Chem. Soc.* **2011**, *133*, 17444−17453.
(52) Peng, J.; Hu, M.; Guo, S.; Du, Z.; Zheng, J.; Shang, D.; Zamora, M. L.; Zeng, L.; Shao, M.; Wu, Y.-S.; Zheng, J.; Wang, Y.; Glen, C. R.; Collins, D. R.; Molina, M. J.; Zhang, R. Markedly enhanced absorption and direct radiative forcing of black carbon under polluted urban environments. *Proc. Natl. Acad. Sci. U. S. A.* **2016**, *113*, 4266−4271.
(53) Pagels, J.; Khalizov, A. F.; McMurry, P. H.; Zhang, R. Y. Processing of soot by controlled sulphuric acid and water condensation-mass and mobility relationship. *Aerosol Sci. Technol.* **2009**, *43*, 629−640.
(54) Khalizov, A. F.; Zhang, R.; Zhang, D.; Xue, H.; Pagels, J.; McMurry, P. H. Formation of highly hygroscopic soot aerosols upon internal mixing with sulfuric acid vapor. *J. Geophys. Res.* **2009**, *114*, D05208.
(55) Zhang, R.; Wang, G.; Guo, S.; Zamora, M. L.; Ying, Q.; Lin, Y.; Wang, W.; Hu, M.; Wang, Y. Formation of urban fine particulate matter. *Chem. Rev.* **2015**, *115*, 3803−3855.
(56) Khalizov, A. F.; Cruz-Quinones, M.; Zhang, R. Heterogeneous reaction of NO_2 on fresh and coated soot surfaces. *J. Phys. Chem. A* **2010**, *114*, 7516−7524.

DOI: 10.1021/acscatal.7b04195
ACS Catal. 2018, 8, 3825−3832